Volume 1 | Number 1 | Jan 2013 | Pages 1–100

Nanoscale

www.rsc.org/nanoscale

ROYAL SOCIETY OF CHEMISTRY

ROYAL SOCIETY OF CHEMISTRY

www.rsc.org/nanoscale

Few-layered MoS$_2$ Nanosheets Wrapped Ultrafine TiO$_2$ Nanobelts with Enhanced Photocatalytic Property

Haidong Li[1¶], Yana Wang[1¶], Guohui Chen[1], Yuanhua Sang[1], Huaidong Jiang[1], Jiating He[2], Xu Li[2*] and Hong Liu[1*]

1. State Key Laboratory of Crystal Materials, Shandong University, Jinan ,China 250100

2. Institute of Materials Research and Engineering, A*STAR, 2 Fusionopolis Way, Innovis, #08-3, Singapore 138634.

¶ These authors have contributed equally to this work.

* Corresponding authors: hongliu@sdu.edu.cn (H. Liu), x-li@imre.a-star.edu.sg (X. Li)

Abstract

Photocatalytic materials comprised of semiconductor nanostructures have attracted tremendous scientific and technological interest over 30 years. This is due to the fact that the photocatalytic materials have unique properties that allow for an effective direct energy transfer from light to highly reactive chemical species which are applicable in remediation of environmental pollutants and photocatalytic hydrogen generation. Heterostructured photocatalysts is a promising type of photocatalyst which can combine the property of different components and probably generate synergic effect, resulting in high photocatalytic activity. In this work, heterostructured photocatalyst comprised of few-layered MoS_2 nanosheets coated on TiO_2 nanobelt surface were synthesized through a simple hydrothermal treatment. The hybrid heterostructures with enhanced broad spectrum photocatalytic properties can harness UV and visible light energy to decompose organic contaminants in aqueous solutions as well as split water to hydrogen and oxygen. The mechanism of the enhancement is that the MoS_2/TiO_2 nanobelt heterostructure can enhance the separation of the photo-induced carriers, which results in a higher photocurrent due to the special electronic characteristics of graphene-like layered MoS_2 nanosheets. This methodology is potentially applicable to the synthesis of a range of hybrid nanostructures with promising applications in photocatalysis and relevant areas.

Introduction

The environmental issues and energy crisis are becoming serious challenge for society as they block up economic growth and contaminate water resources, endangering both wildlife and human life[1]. Recently, semiconductor photocatalysts have been widely investigated on decomposition of toxic and hazardous organic pollutants as well as generation of hydrogen for solving environmental and energy problem[2-4]. Over the last 30 years, photocatalytic materials based on Titanium dioxide (TiO_2) have attracted tremendous scientific and technological interest. The origin of the vast majority of these efforts is due to the fact that TiO_2 has a unique set of properties that allow for an effective direct energy transfer from light to highly reactive chemical species[5-7]. These features can be exploited to tackle several contemporary global challenges involving pollutant degradation and the direct splitting of water into H_2 and O_2. However, on one hand, TiO_2 can only absorb ultraviolet (UV) light which accounts for only about 4% of the sunlight energy due to its large bandgap (3.2 eV for anatase), greatly impeding its widespread applications[8, 9]; On the other hand, charge carrier recombination can reduce the photocatalytic activity of TiO_2[10-12]. Therefore, charge separation also plays a key role in determining solar energy conversion efficiency of TiO_2-based systems.

Heterostructured photocatalyst is one of the most popular structures for enhanced photocatalytic activity[13-23]. Heterostructured photocatalysts have a better performance than either of the parent phases. The presence of the heterojunctions changes the band bending at interfaces and provides a driving force for the separation of photogenerated electrons and holes, so that the photocatalysts with heterojunctions can mitigate the effects of carrier recombination and back-reaction, which in turn increases photochemical reactivity[1, 9, 24]. Therefore, incorporating semiconductor with suitable cocatalysts to form

heterostructured photocatalysts is a promising approach for achieving high photocatalytic reactivity. Suitable cocatalysts loaded on the surface of TiO_2 photocatalysts can be served as active centers for pollutant degradation as well as H_2 or O_2 generation. Noble metals such as Pt, Ru, Rh, Au, Ag and their corresponding oxides are one type of common cocatalysts[13, 15, 25-27]. Among them, Pt appears to be the best catalyst and is widely used for H_2 production. However, the high cost and limited resource hinders its practical application. To overcome these challenges, much effort has been directed toward the exploitation of Pt-free materials and molybdenum disulfide (MoS_2) has been proven to be an effective cocatalyst to be integrated with TiO_2 for photocatalysis[24, 28-31].

MoS_2 has a graphene-like layered structure with anisotropy, chemically inertness, electroconductivity, photo-corrosion resistance and specific optical properties [29, 32]. Recently, several studies on MoS_2-TiO_2 composites for H_2 production or photocatalytic degradation of pollutants have been reported: (1) MoS_2 nanoparticles were used as cocatalysts to incorporate with P25 (a commercial TiO_2 product) to form MoS_2/P25 nanoparticles or ultrafine TiO_2 nanoparticles with diameters in the range of 5−8 nm to form MoS_2/TiO_2 nanoparticles, which were employed as hybrid nanophotocatalysts in photo-oxidative removal of phenol from aqueous solution[33] or photocatalytic H_2 production[34, 35]. Such nanocomposites show superior photocatalytic activity, but, the collection cost of the nanocomposites from suspension after reaction is even higher than the price of the TiO_2 precursors. (2) MoS_2–TiO_2 hybrid catalysts synthesized via mechanochemistry[36] or chemically exfoliated metallic MoS_2 nanosheets method[37], exhibit excellent performance in both photocatalytic H_2 production and Rhodamine B (RhB) degradation, but the process is complicated and the photocatalytic efficiency is

low. (3) TiO_2 nanobelts modified with MoS_2 nanoparticles or nanosheets show high photocatalytic activity[38, 39]. However, the nanobelts synthesized via an alkaline hydrothermal method without an acid etching process exhibit a smooth surface with small specific surface area (26 ± 5 $m^2 \cdot g^{-1}$) and less active facets, holding up its photocatalytic activity. With an acid etching process, TiO_2 nanobelts have larger specific surface area and more active facets, but the etching process is complicated and the utilization rate of TiO_2 nanobelts is reduced.

In this paper, ultrafine TiO_2 nanobelts with high specific surface area (72.2 $m^2 \cdot g^{-1}$) were synthesized through a simple hydrothermal treatment. Compared with the conventional TiO_2 nanobelts synthesized via an alkaline hydrothermal-based method, the size of the ultrafine TiO_2 nanobelts is reduced by an order of magnitude. Hybrid MoS_2/TiO_2 nanobelt heterostructures were prepared by wrapping few-layered MoS_2 nanosheets on TiO_2 nanobelts, which enhances UV-visible light-driven photocatalytic activity. Owing to the heterostructures comprised of MoS_2 nanosheets and ultrafine TiO_2 nanobelts, the adsorption of dye molecules and separation ability of photo-induced carriers is enhanced obviously, which endows MoS_2/TiO_2 nanobelt heterostructure a high photocatalytic efficiency in both UV and visible light regions for H_2 evolution and photocatalytic degradation of organic pollutants. Due to the facile synthetic process, low cost, and especially the high photocatalytic property, this ultrafine MoS_2/TiO_2 nanobelt heterostructures show potential in applications in both photodegradation of pollutants and H_2 generation.

Experimental section

Chemicals: The chemicals used in this work were of analytical reagent grade. Solutions were freshly prepared with deionized water. Ammonium tetrathiomolybdate (ATM, 99%), lithium acetate (LiAc·2H$_2$O, 98%) and titanium (IV) butoxide (TB, 98%) were purchased from Sigma-Aldrich Co. LLC. N, N-dimethylformamide (DMF, 99%), and acetic acid (HAc, 99%) were purchased from Sinopharm Chemical Reagent Co.,Ltd,. Titania P25 (TiO$_2$, ca. 80% anatase, and 20% rutile, commercialized Degussa P25). All chemicals were used without further purification.

Synthesis of ultrafine TiO$_2$ nanobelts

In a typical synthesis, 0.2 g of LiAc·2H$_2$O was dissolved in 10 mL of a mixed DMF/HAc organic solvent with ratio of 6/4(v/v). After mixing with 2 mL of TB, the solution was transferred into a Teflon-lined stainless steel autoclave, and heated in an oven at 200 °C for 20 h. Finally, the product was collected and washed thoroughly with ethanol for several times, and dried in a vacuum oven at 60 °C overnight to obtain the ultrafine TiO$_2$ nanobelts[5].

Synthesis of MoS$_2$ nanosheets and MoS$_2$/TiO$_2$ nanobelt heterostructures

Layered MoS$_2$ nanosheets were synthesized by hydrothermal treatment. 50 mmol of ATM powder was dissolved in 80 ml of distilled water under stirring. The solution was transferred into a Teflon-lined stainless steel autoclave and heated at 200 ° C for 24 h. After cooling down to room temperature, the black precipitates were collected and washed with distilled water and ethanol in turn. After dried at 60 ℃ for 12 hours, MoS$_2$ nanosheets were successfully synthesized[31].

The hybrid MoS_2 /TiO_2 nanobelt heterostructures were synthesized by hydrothermal treatment. 5 mmol of ATM powder was dissolved in 80 ml of distilled water, 100 mmol of ultrafine TiO_2 nanobelts was added into the solution, then stirred for 0.5 hour. The solution was stirred and then transferred into a Teflon-lined stainless steel autoclave, heated at 200 °C for 24 h. After cooling down to room temperature, the brunette precipitates were collected and washed with distilled water and ethanol in turn. After drying at 60 ºC for 12 hours, MoS_2/TiO_2 nanobelt heterostructures (5 % of MoS_2) were synthesized.

Characterization: X-ray powder diffraction (XRD) patterns were recorded on a Bruke D8 Advance powder X-ray diffractometer at 40 kV and 40 mA with monochromatized Cu Kα (λ = 0.15406 nm). Field emission scanning electron microscopy (FESEM, HITACHI S-4800) and high resolution transmission electron microscopy (HRTEM, JOEL JEM 2100F) were used to observe the morphology and size of the synthesized samples. The chemical composition was investigated by the energy dispersive X-ray spectroscopy (EDX). X-ray photoelectron spectroscopy (XPS) was performed using an ESCALAB 250. UV-visible absorption spectra were recorded on a UV-visible spectrophotometer (UV-2550, Shimadzu) with an integrating sphere attachment within the range of 200 to 800 nm and using $BaSO_4$ as the reflectance standard. Raman spectroscopy was performed at room temperature with a Raman spectrometer (Witec CRM200) at an excitation wavelength of 473 nm and a power of 22 mW; the exposure time was 20 s/scan for 20 scans. Fourier-transform infrared (FT-IR) spectra were collected on a Nicolet Avatar 370 infrared spectrometer in the range of 400-4000 cm^{-1} using pressed KBr discs. The KBr pellets were prepared where 10 mg of a sample was

mixed with 1000 mg of KBr in an agate mortar. From this stock, 200 mg were then pressed into pellets of 13 mm in diameter.

Photocurrent measurements: For the fabrication of the photoelectrodes, 1 mL of an terpineol suspension of the as-prepared photocatalyst powders (20 mg) was dip-coated onto a piece of the fluorine-doped tin oxide (FTO) glass substrate with a cover area of 1 cm^2 and allowed to dry under ambient condition. The photocurrent was measured with an electrochemical workstation (CHI 750E, CH Instruments Inc., Shanghai) using a three-electrode mode in 1 M aqueous solution of Na_2SO_4. The reference electrode and counter electrode were Ag-AgCl electrode (saturated KCl) and platinum wire, respectively. The as-prepared photoelectrodes were used as the anodes for the electrochemical characterization[36, 40].

Photocatalytic Test: The photocatalytic activity of MoS_2/TiO_2 nanobelt heterostructures was assessed by the photodegradation of methylene orange (MO) using photochemical reaction apparatus. In a typical experiment, 20 mL aqueous suspensions of MO (20 mg·L^-^{1}) and 20 mg of sample were placed in a 50 mL beaker. Prior to irradiation, the suspensions were magnetically stirred in the dark for 30 min to establish adsorption/desorption equilibrium between the dye and the surface of the catalyst at room temperature. A 300 W mercury lamp with a maximum emission of 356 nm was used as the UV light source and a 350 W Xe lamp with a cut-off filter ($\lambda > 420$ nm) was used as the visible light source. For comparison, photodegradation capabilities of 20 mg TiO_2 nanobelts and 20 mg MoS_2 nanosheets were evaluated under the same experimental condition. At varied irradiation time intervals, the residual MO concentration in the supernatant was analyzed by UV-visible spectroscopic measurement (Hitachi UV-3100).

The H$_2$ evolution experiments were carried out in a gas closed circulation system. In a typical reaction, 100 mg of the catalyst powder was dispersed in CH$_3$OH aqueous solution using a magnetic stirrer (80 mL of distilled water and 20 mL of CH$_3$OH). A commercial solar simulator (300 W) equipped with a Xe lamp was used as the light source for photocatalytic H$_2$ generation. The power density of the incident light was about 100 mW·cm^{-2}. Hydrogen gas was measured by an on-line gas chromatography (GC-7900, Argon as a carrier gas) equipped with thermal conductivity detector (TCD).
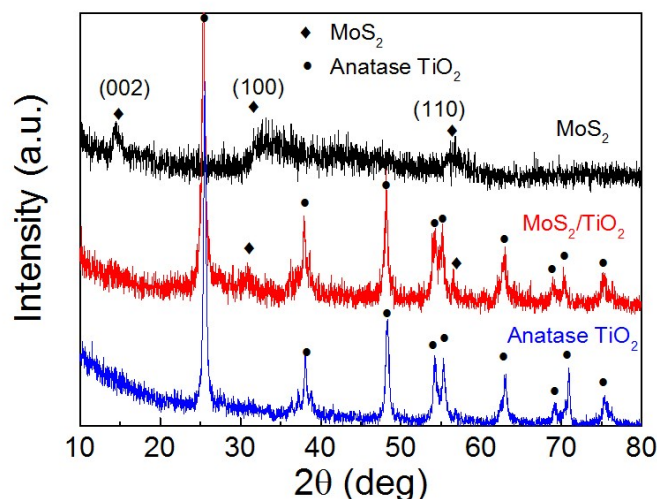
Result and discussion

Figure 1 XRD patterns of ultrafine TiO$_2$ nanobelts, pure MoS$_2$ nanosheets and

MoS$_2$/TiO$_2$ nanobelt heterostructures (5 % of MoS$_2$).

The X-ray powder diffraction (XRD) patterns of as-prepared TiO$_2$ nanobelts, pure MoS$_2$ nanosheets and MoS$_2$/TiO$_2$ nanobelt heterostructures (5 % of MoS$_2$) are shown in Figure 1. The diffraction peaks of the ultrafine TiO$_2$ nanobelts (Blue curve in Figure 1) match

the standard peaks of anatase phase (JCPDS card no. 21-1272). As for the pure MoS_2

nanosheet sample (Black curve in Figure 1), the detected peaks can be assigned to the

(002), (100) and (110) planes in the hexagonal phase MoS_2 (a = b = 0.316 nm, c = 1.230

nm, JCPDS card no. 37-1492). The peak at 14.5° shown in the pure MoS_2 powder was

not observed in the XRD pattern of the MoS_2/TiO_2 heterostructure (Red curve in Figure

1). This diffraction peak is corresponding to the c-plane of MoS_2 which is composed of

Mo atoms coordinated with S atoms, forming a S-Mo-S sandwich structure. The absence

of this peak (~14.5°) indicates that MoS_2 nanosheets coated on the TiO_2 nanobelts

probably contain only a few of layers, which are too thin to be detected by XRD.

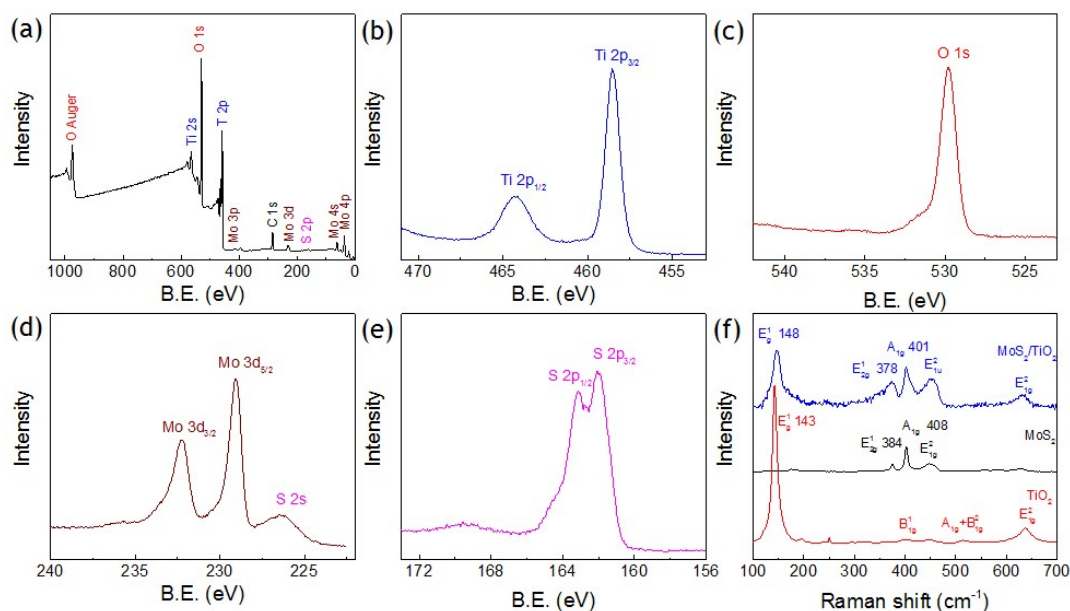Figure 2 XPS spectra of MoS_2/TiO_2 nanobelt heterostructures:

(a) Survey spectra of MoS_2/TiO_2, enlarged signals of (b) Ti2p, (c) O1s, (d) Mo3d and (e)

S2p. (f) Raman spectra of TiO_2, MoS_2, and MoS_2/TiO_2 nanobelt heterostructures.

The chemical composition and valence state were characterized by X-ray photoelectron spectroscopy (XPS). The full range of XPS spectra of MoS_2/TiO_2 (0–1050 eV) are shown in Figure 2a. Figure 2b shows that the binding energy (BE) of $Ti2p_{3/2}$ and $Ti2p_{1/2}$ are 458.3 and 464.1 eV respectively, which are ascribed to the Ti^{4+} oxidation state. In Figure 2c, O1s is observed and it is useful in identifying the core levels[40]. As shown in Figure 2d and 2e, the high-resolution XPS spectra show that the binding energy of $Mo3d_{3/2}$, $Mo3d_{5/2}$, $S2p_{1/2}$ and $S2p_{3/2}$ peaks in the MoS_2/TiO_2 nanobelt heterostructures are located at 232, 228.8, 162.9 and 161.9 eV, respectively. According to a report published by wang *et al.*[41], the binding energy of pure layered MoS_2 nanosheets should be located at 232.5, 229.3, 163.3 and 162.3 eV. Thus, it suggests that binding energy of $Mo3d_{5/2}$, $Mo3d_{3/2}$, $S2p_{1/2}$ and $S2p_{3/2}$ for the MoS_2/TiO_2 nanobelt heterostructures shift to lower energy states after MoS_2 nanosheets were wrapped on the TiO_2 nanobelts. The shift of the peaks could be attributed to the heterostructure effect between the MoS_2 nanosheets and TiO_2 nanobelts [39, 41].

To further explore the properties of the hybrid nanostructures, phonon spectra of TiO_2, MoS_2, and MoS_2/TiO_2 hybrid structures were measured by Raman scattering (Figure 2f). The phonon vibrational modes of the ultrafine TiO_2 nanobelt at 148 cm^{-1}, 397 cm^{-1}, 518 cm^{-1} and 638 cm^{-1} correspond to the E_g^1, , B_{1g}^1, $A_{1g}+ B_{1g}^2$ and E_g^2 modes of anatase TiO_2, respectively[42, 43]. The Raman scattering peaks of the pure MoS_2 nanosheets observed at 384 cm^{-1}, 408 cm^{-1} and 452 cm^{-1} can be assigned to the representative modes of E_{2g}^1, A_{1g}, and , E_{1U}^2, respectively[26, 28, 44, 45]. In the Raman spectrum of the MoS_2/TiO_2 hybrid nanostructures, there is a blue shift of 5 cm^{-1} observed with the E_g^1 mode compared to that of the ultrafine TiO_2 nanobelts, mostly due to a surface strain induced by the wrapped

MoS$_2$ nanosheets on the TiO$_2$ surface[39]. Meanwhile, there is also a surface strain generated in the wrapped MoS$_2$ nanosheets, which leads to the red shifts of 6 and 7 cm^{-1} for the E$_{2g}^1$ and A$_{1g}$ modes, respectively, compared to the pure MoS$_2$ nanosheets. The shell configuration of the MoS$_2$ nanosheets leads to a tensile strain along the (001) plane and a compressive strain in the basal plane. This tensile strain along the (001) direction reduces the van der Waals forces between neighboring layers, which causes a decrease in restoring force. Therefore, a decrease is observed in vibrational frequencies of both of the E$_{2g}^1$ and A$_{1g}$. With regards to the crystal structure, the phonon spectra of the hybrid structures confirm the coating of MoS$_2$ nanosheet on TiO$_2$ nanobelts surface.
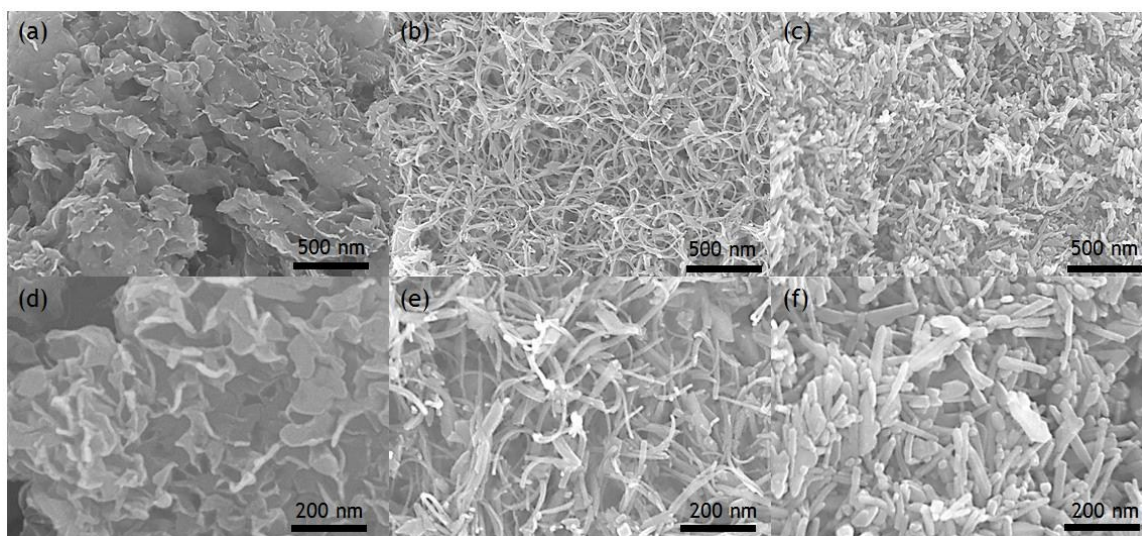

Figure 3 SEM images of (a,d) MoS$_2$ nanosheets, (b,e) TiO$_2$ nanobelts and (c,f) MoS$_2$/TiO$_2$ nanobelt heterostructures (5% of MoS$_2$).

Figure 3 presents the corresponding scanning electron microscopy (SEM) images of MoS$_2$ nanosheets, TiO$_2$ nanobelts and MoS$_2$/TiO$_2$ nanobelt heterostructures (5% of MoS$_2$) obtained by the hydrothermal treatment, respectively. MoS$_2$ nanosheets were successfully synthesized and the morphology is characterized by SEM as shown in Figure 3a and 3d, a

layered-like MoS$_2$ sample with a high crystallinity is obtained. Figure 3b and 3e shows

the ultrafine TiO$_2$ nanobelts have a uniform morphology and a well dispersion and the

surface of ultrafine TiO$_2$ nanobelts is very smooth with a typical length of several

hundred nanometers and width of 15-20 nm. After MoS$_2$ nanosheets grown on TiO$_2$

nanobelts, the thin MoS$_2$ nanosheets are uniformly coated on the TiO$_2$ nanobelts. Typical

SEM images of MoS$_2$/TiO$_2$ nanobelt heterostructures (with 5 % of MoS$_2$) are shown in

Figure 3c and 3f. Compared to the original TiO$_2$ nanobelts, the surface of MoS$_2$/TiO$_2$

nanobelt heterostructures become slightly rough and their width increases to 20-25 nm

(see Figure 4f). The result shows that MoS$_2$/TiO$_2$ nanobelt heterostructures are prepared
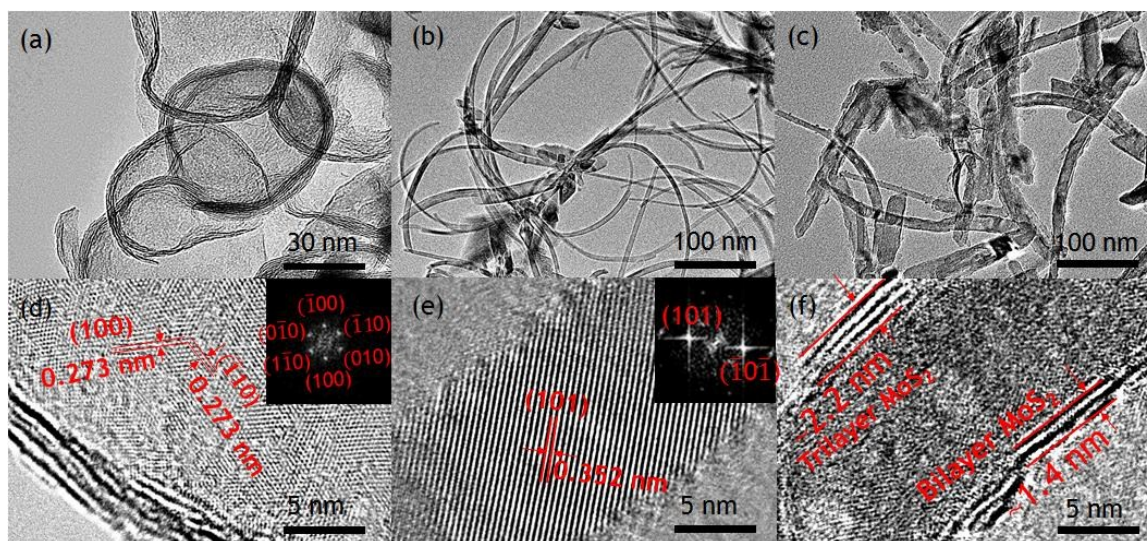
successfully.

Figure 4 TEM images of (a) MoS$_2$ nanosheets, (b) TiO$_2$ nanobelts and (c) MoS$_2$/TiO$_2$

nanobelt heterostructures (5% of MoS$_2$). HRTEM images of (d) MoS$_2$ nanosheets, (e)

TiO$_2$ nanobelts and (f) MoS$_2$/TiO$_2$ nanobelt heterostructures (5% of MoS$_2$). Inset in (d)

and (e): the corresponding fast fourier transform electron diffraction pattern of MoS_2 and

TiO_2.

High resolution transmission electron microscopy (HRTEM) is employed to further

characterize the structures of the products. Figure 4 shows the morphology and

nanostructure of the MoS_2 nanosheets, TiO_2 nanobelts and MoS_2/TiO_2 nanobelt

heterostructures (5% of MoS_2). As shown in Figure 4a, the pure MoS_2 crystals generally

appear to be plate-like structure with a diameter as large as 60 nm, probably formed by

the primary MoS_2 layers with edge curl. It can be clearly observed from Figure 4d that

the MoS_2 nanosheets exhibit a wavy shape and have a well-layered-like structure. From

the HRTEM images in Figure 4d, the lattice fringes of MoS_2 nanosheets can be clearly

observed, suggesting the well-defined crystal structure. The fringes with a lattice spacing

of 0.273 nm corresponding to the (100) plane of MoS_2 (the corresponding Fast Fourier

Transformation (FFT) pattern insets)[39, 46]. Figure 4b clearly reveals that the TiO_2 have

belt-like nanostructures with good flexibility. The width of the TiO_2 nanobelts was

measured as about 10-12 nm from tiled nanobelts, and the thickness of the nanobelts is

estimated at about 3-5 nm from the narrowest part of kinked nanobelts. HRTEM image of

part of a typical nanobelt is depicted in Figure 4e (see TEM image of kinked TiO_2

nanobelt in Supporting Information S1). The width of TiO_2 nanobelts is further affirmed

as about 10 nm. The uniform lattice fringes of the nanobelt indicate the high crystallinity

and the FFT pattern shows that the (001) plane of nanobelt grows along [010] direction.

The lattice fringes with inter-plane spacing of 0.352 nm also point out the growth

direction of the nanobelt. As shown in Figure 4c and 4f, the structure of the MoS_2/TiO_2

nanobelt heterostructures was also characterized by HRTEM, which shows that the

hybrid nanostructures keep the belt-like shape. (see more HRTEM images of MoS_2/TiO_2 nanobelt heterostructures in Supporting Information S1). However, the width and thickness of the nanobelts increases to about 15-20 nm and 5-8 nm, respectively. As shown in Figure 4f, a phase with layered crystal structure wrapped on the surface of ultrafine TiO_2 nanobelts is present. In this layered structure, the distance of the two adjacent fringes is about 0.7 nm, which is corresponding to the distance between two c planes of MoS_2 sheets. Combined with the XRD results, it is confirmed that the layered nanostructure on the surface of ultrafine TiO_2 nanobelt should be MoS_2. Furthermore, we can find that only two or three layers of MoS_2 wrapped on the surface of ultrafine TiO_2 nanobelts. In addition, the crystal structure of ultrafine TiO_2 nanobelt is not uniform along the nanobelt and parts of them are disordered, as a result of the compression stress caused by the difference of thermal expansion coefficient (9.00×10^{-6} K^{-1} for TiO_2, 8.65×10^{-6} K^{-1} for MoS_2) [47, 48]. To further confirm the surface layer is MoS_2, energy dispersive X-ray spectrometry (EDS) mapping and scanning transmission electron microscope (STEM) (Figure 5) analysis of the MoS_2/TiO_2 nanobelt heterostructures were conducted. EDS pattern of MoS_2/TiO_2 nanobelt heterostructures shows that the product nanobelts is composed of Ti, O, Mo and S (Detailed discussion can be found in Supporting Information S2). The EDS elemental mapping supports our argument that the outer layer is MoS_2 nanosheets and the inner layer is TiO_2 nanobelt. The above experimental results prove that an active facet (001) is exposed on the surface of ultrafine TiO_2 nanobelts [6, 49], and only a few layers of MoS_2 are wrapped on the surface of ultrafine TiO_2 nanobelt, to form MoS_2/TiO_2 nanobelt heterostructures.
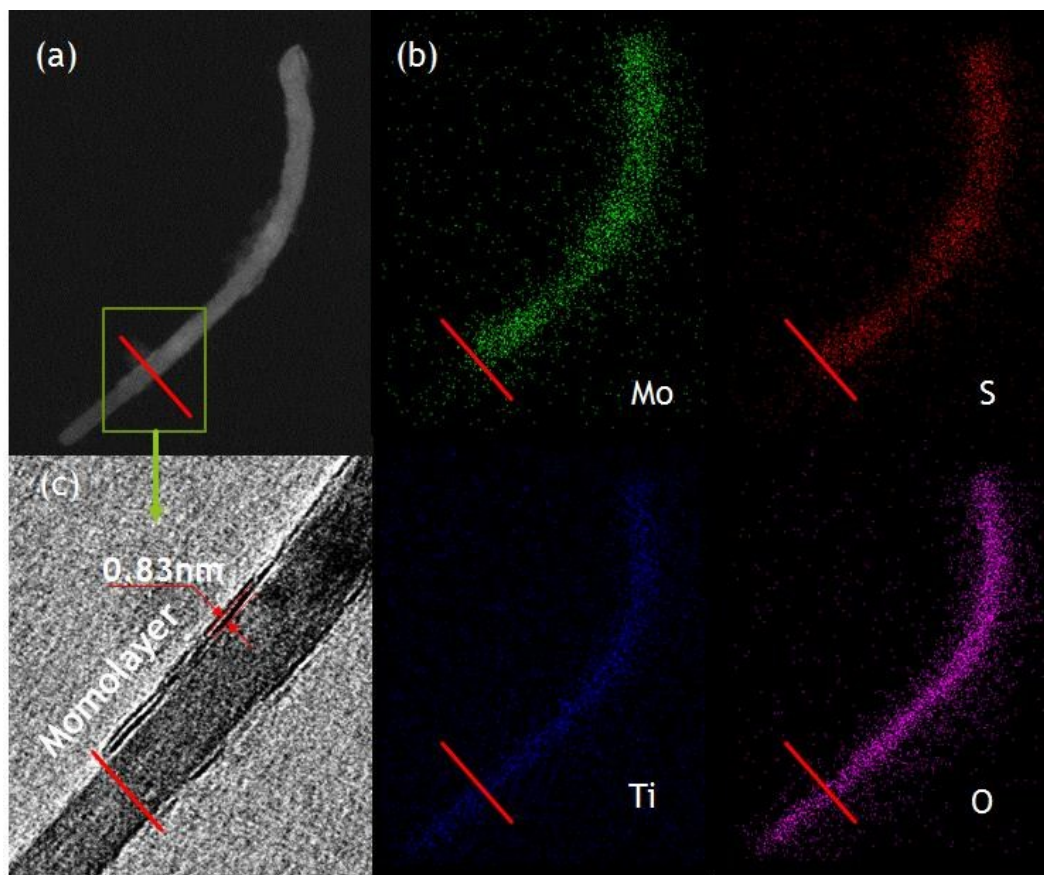
Figure 5 (a) STEM image, (b) EDS mapping results from MoS_2/TiO_2 nanobelt heterostructures (5% of MoS_2), (c) the corresponding TEM image of MoS_2/TiO_2 nanobelt heterostructures from (a).
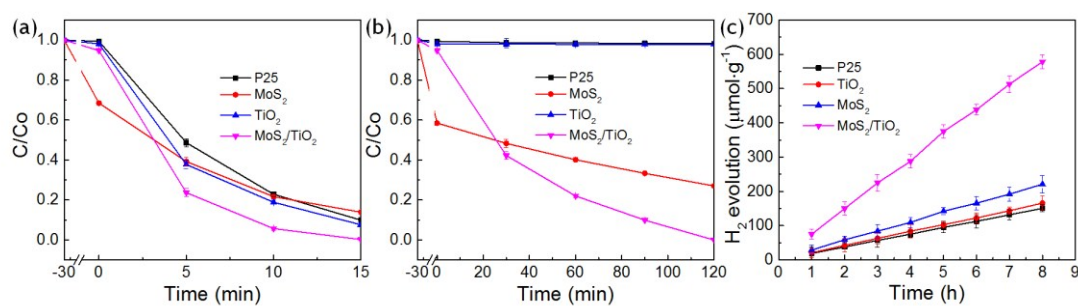

Figure 6 Photocatalytic degradation of MO in the presence of P25, TiO_2 nanobelts, MoS_2 nanosheets and MoS_2/TiO_2 hybrid nanobelt (5%, MoS_2) under either (a) UV or (b) visible

light irradiation. (c) Photocatalytic H_2 evolution from an aqueous methanol solution over

P25, TiO_2 nanobelts, MoS_2 nanosheets and MoS_2/TiO_2 hybrid nanobelt heterostructures

(5%, MoS_2).

To evaluate the photocatalytic performance of MoS_2/TiO_2 nanobelt heterostructures (5%,

MoS_2), the degradation of methylene orange (MO) in water under UV or Visible light

irradiation as a function of time was investigated (Figure 6a and 6b). P25, ultrafine TiO_2

nanobelts, MoS_2 nanosheets were used as references. As shown in Figure 6a, in the

presence of pure P25, about 91.0% of MO is degraded within 15 min, while the

degradation ratio is of 92.4% in the presence of the ultrafine TiO_2 nanobelts. This may be

attributed to the large amount of the exposed active facets on the surface of ultrafine TiO_2

nanobelts. However, it is difficult to prepare exposed active facets in traditional TiO_2

nanobelts through an alkaline hydrothermal method[1, 2, 10, 13, 14, 50]. Surprisingly, for the

MoS_2/TiO_2 nanobelt heterostructures, MO can be completely degraded within 15 min.

The degradation activity of MoS_2/TiO_2 nanobelt heterostructures is much stronger than

that of P25, ultrafine TiO_2 nanobelts and MoS_2 nanosheets. As mentioned above, MoS_2 is

not a good UV active photocatalyst, thus the enhanced UV photocatalytic activity of

MoS_2/TiO_2 hybrid nanobelt composites should be attributed to the heterostructure of

MoS_2/TiO_2 nanobelt heterostructures.

The visible-light photocatalytic activity of P25, TiO_2 nanobelts, MoS_2 nanosheets and

MoS_2/TiO_2 nanobelt heterostructures (5%, MoS_2) is also evaluated by studying

photocatalytic degradation of MO aqueous solution under visible-light irradiation (Figure

6b). As shown in Figure 6b, P25 and ultrafine TiO_2 nanobelts have a low photocatalytic

activity under visible light, and the degradation is only ca. 2% in 120 min due to the large

band gap energy of 3.2 eV (anatase) of TiO_2. Thus, the photocatalytic reaction of TiO_2 proceeds only at wavelength shorter than approximately 400 nm[1, 2, 5, 39, 44]. However, the pure MoS_2 nanosheets have a relatively good visible-light photocatalytic activity and the corresponding degradation of MO reaches 73.1% in 120 min. Surprisingly, the MoS_2/TiO_2 nanobelt heterostructures demonstrated strongest the visible-light photocatalytic activity and the MO can be completely degraded by MoS_2/TiO_2 nanobelt heterostructures in 120 min. More details about the degradation of MO by MoS_2/TiO_2 nanobelt heterostructures are discussed in Supporting Information S3.

To further investigate the enhanced photocatalytic property of the MoS_2/TiO_2 nanobelt heterostructures, the evolution of H_2 was measured in the presence of the as-synthesized samples under simulated sunlight irradiation. As shown in Figure 6c, the amount of H_2 increases linearly with the irradiation time (over 8 h) for P25, TiO_2 nanobelts, MoS_2 nanosheets and MoS_2/TiO_2 nanobelt heterostructures. The H_2 generation rate of the MoS_2/TiO_2 nanobelt heterostructures is about 75 $\mu mol \cdot h^{-1} \cdot g^{-1}$, while the H_2 generation rate of P25, TiO_2 nanobelts and MoS_2 nanosheets is about 29 $\mu mol \cdot h^{-1} \cdot g^{-1}$, 21 $\mu mol \cdot h^{-1} \cdot g^{-1}$, and 19 $\mu mol \cdot h^{-1} \cdot g^{-1}$, respectively. Moreover, after four cycles of 8 h reaction, the MoS_2/TiO_2 nanobelt heterostructures still retained high photocatalytic activity (Supporting Information S4). These results indicate that the MoS_2/TiO_2 nanobelt heterostructures have the highest photocatalytic activity among these materials.

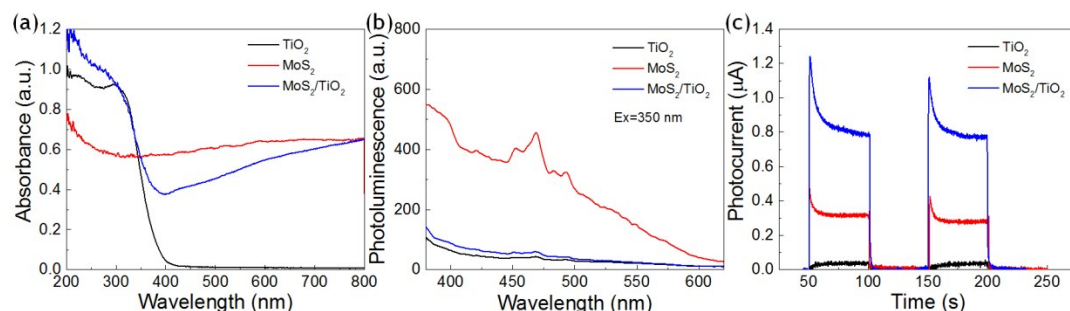Figure 7 (a) UV-visible diffuse reflectance spectra and (b) Photoluminescence spectra

(Ex=350 nm) of ultrafine TiO_2 nanobelts, MoS_2 nanosheets and MoS_2/TiO_2 nanobelt

heterostructures (5%, MoS_2). (c) Photocurrent response for ultrafine TiO_2 nanobelts,

MoS_2 nanosheets and MoS_2/TiO_2 nanobelt heterostructures (5%, MoS_2, 0.05 V bias)

under simulated solar light illumination. All of the photocurrent intensities were

calibrated with dark current.

To investigate the optical properties, the as-prepared samples were analyzed by UV-
visible diffuse reflectance spectra (DRS) and photoluminescence spectra (PL). The DRS
of ultrafine TiO_2 nanobelts, MoS_2 nanosheets and MoS_2/TiO_2 nanobelt heterostructures
(5%, MoS_2) are shown in Figure 7a. The ultrafine TiO_2 nanobelts show a sharp
fundamental absorption edge at about 380 nm, while the layered MoS_2 nanosheets show
increased absorption in the UV-visible region. Expectedly, the visible absorption
intensity of MoS_2/TiO_2 photocatalysts were enhanced significantly after MoS_2 nanosheets
were coated on ultrafine TiO_2 nanobelts, resulting in higher light energy utilization.
Therefore, the few-layer MoS_2/TiO_2 nanobelt heterostructures absorbed more photons for
photocatalytic reactions.

Photoluminescence (PL) is often employed to study the surface structure and excited state
of semiconductors. Upon electron–hole pair recombination after being irradiated,

semiconductor emits photons, resulting in PL emission. Figure 7b shows the photoluminescence spectra of ultrafine TiO_2 nanobelts, MoS_2 nanosheets, and MoS_2/TiO_2 nanobelt heterostructures. The PL emission spectrum of MoS_2 nanosheets shows a wide emission peak centered at ca. 460 nm, which corresponds to the direct band-to-band radiative recombination of photogenerated electrons and holes[10, 14, 50]. After integrated with TiO_2 to form MoS_2/TiO_2 nanobelt heterostructures, the PL intensity of the products decreases significantly which indicates a drastic fluorescence quenching effect of TiO_2. This result suggests that the recombination of photogenerated electrons and holes is effectively suppressed in MoS_2/TiO_2 nanobelt heterostructures. Due to the favorable electrical conductivity, MoS_2 nanosheets here work as an electron mediator and transporter for improving the charge separation efficiency, thus leading to much enhanced photocatalytic activity [34, 37-39, 51].

To further investigate the enhancement of the photocatalytic property of the MoS_2/TiO_2 nanobelt heterostructures, the photoelectrochemical performance of ultrafine TiO_2 nanobelts, MoS_2 nanosheets and MoS_2/TiO_2 nanobelt heterostructures (5%, MoS_2) were measured under 0.05 V bias. Figure 7c shows the Photocurrent–Time measurements to examine the photocurrent response of the samples over cycles of light on-off under 0.05 V bias. When the irradiation is interrupted, the photocurrent rapidly dropped to almost zero (steady-state value), and the photocurrent reverted back to its original value once the light was switched on again. The photocurrent of the TiO_2 nanobelt and the MoS_2 nanosheet anode is about 0.05 $\mu A \cdot cm^{-2}$ and 0.33 $\mu A \cdot cm^{-2}$, respectively. Surprisingly, the photocurrent of the MoS_2/TiO_2 hybrid nanobelt anode approaches 0.79 $\mu A \cdot cm^{-2}$, which is more than twice of the MoS_2 anode. The significant photocurrent enhancement was

ascribed to the improved charge separation in the few-layered MoS_2/TiO_2 nanobelt heterostructure. The proposed mechanism shown in in Supporting Information S5 for the enhanced electron transfer in the MoS_2/TiO_2 nanobelt heterostructures under irradiation assumes that the photoexcited electrons are transferred from the conduction band of outer MoS_2 nanosheets to inner TiO_2 nanobelts, which can effectively separate photogenerated electrons and holes and promote the photo-induced oxidation-reduction reaction.

Conclusions

Heterostructured few-layered MoS_2/TiO_2 nanobelt heterostructures were synthesized by wrapping ultrathin anatase TiO_2 nanobelts with MoS_2 nanosheets through hydrothermal treatment. The few-layered of MoS_2 nanosheets coated onto TiO_2 nanobelts not only broaden the photocatalytic light region from UV to visible, but also enhances the photocatalytic activity of the nanobelt heterostructures due to band matching between MoS_2 and TiO_2. With high electrical conductivity, MoS_2 nanosheets here work as an electron mediator and transporter for improving the charge separation efficiency and heterojunctions in the MoS_2/TiO_2 nanobelt heterostructures can effectively improve charge separation of the few-layered MoS_2/TiO_2 nanobelt heterostructures, leading to much enhanced photocatalytic activity. These ultrafine TiO_2 nanobelt based MoS_2/TiO_2 heterostrctures not only possesses very high photocatalytic activity in UV-visible region, but also have a good recyclability compared with P25 or other granular nano-photocatalysts, which is a promising candidate in water splitting to generate H_2 and water treatment.

Acknowledgements

1. J. Tian, Z. Zhao, A. Kumar, R. I. Boughton and H. Liu, *Chem. Soc. Rev.*, 2014, **43**, 6920-6937.
2. J. Tian, Y. Sang, G. Yu, H. Jiang, X. Mu and H. Liu, *Adv. Mater.*, 2013, **25**, 5075-5080.
3. A. Mukherji, R. Marschall, A. Tanksale, C. Sun, S. C. Smith, G. Q. Lu and L. Wang, *Adv. Funct. Mater.*, 2011, **21**, 126-132.
4. A. Mukherji, B. Seger, G. Q. Lu and L. Wang, *ACS Nano*, 2011, **5**, 3483-3492.
5. H. B. Wu, H. H. Hng and X. W. Lou, *Adv. Mater.*, 2012, **24**, 2567-2571.
6. C. Li, C. Koenigsmann, W. Ding, B. Rudshteyn, K. R. Yang, K. P. Regan, S. J. Konezny, V. S. Batista, G. W. Brudvig, C. A. Schmuttenmaer and J. H. Kim, *J. Am. Chem. Soc.*, 2015, **137**, 1520-1529.
7. Z. Sun, J. H. Kim, Y. Zhao, F. Bijarbooneh, V. Malgras, Y. Lee, Y. M. Kang and S. X. Dou, *J. Am. Chem. Soc.*, 2011, **133**, 19314-19317.
8. J. Zhang, F. X. Xiao, G. Xiao and B. Liu, *Nanoscale*, 2014, **6**, 11293-11302.
9. F. X. Xiao, S. F. Hung, H. B. Tao, J. Miao, H. B. Yang and B. Liu, *Nanoscale*, 2014, **6**, 14950-14961.
10. J. Tian, Y. Leng, Z. Zhao, Y. Xia, Y. Sang, P. Hao, J. Zhan, M. Li and H. Liu, *Nano Energy*, 2015, **11**, 419-427.
11. J. Bu, J. Fang, W. R. Leow, K. Zheng and X. Chen, *RSC Adv.*, 2015.
12. X. Lang, W. R. Leow, J. Zhao and X. Chen, *Chem Sci*, 2015, **6**, 1075-1082.
13. W. Zhou, H. Liu, J. Wang, D. Liu, G. Du and J. Cui, *ACS Appl. Mater. Inter.*, 2010, **2**, 2385-2392.
14. J. Lin, J. Shen, R. Wang, J. Cui, W. Zhou, P. Hu, D. Liu, H. Liu, J. Wang, R. I. Boughton and Y. Yue, *J. Mater. Chem.*, 2011, **21**, 5106.
15. T. Jiang, C. Jia, L. Zhang, S. He, Y. Sang, H. Li, Y. Li, X. Xu and H. Liu, *Nanoscale*, 2015, **7**, 209-217.
16. B. A. Gonfa, M. R. Kim, N. Delegan, A. C. Tavares, R. Izquierdo, N. Wu, M. A. El Khakani and D. Ma, *Nanoscale*, 2015, **7**, 10039-10049.
17. F. Meng, J. Li, S. K. Cushing, M. Zhi and N. Wu, *J. Am. Chem. Soc.*, 2013, **135**, 10286-10289.
18. G. Liu, L. Wang, C. Sun, X. Yan, X. Wang, Z. Chen, S. C. Smith, H.-M. Cheng and G. Q. Lu, *Chem. Mater.*, 2009, **21**, 1266-1274.
19. G. Liu, L. Wang, H. G. Yang, H.-M. Cheng and G. Q. Lu, *J. Mater. Chem.*, 2010, **20**, 831-843.
20. F. X. Xiao, J. Miao, H. B. Tao, S. F. Hung, H. Y. Wang, H. B. Yang, J. Chen, R. Chen and B. Liu, *Small*, 2015, **11**, 2115-2131.
21. D. Qi, L. Zheng, X. Cao, Y. Jiang, H. Xu, Y. Zhang, B. Yang, Y. Sun, H. H. Hng, N. Lu, L. Chi and X. Chen, *Nanoscale*, 2013, **5**, 12383-12387.

22. Y. Wang, Q. Wang, X. Zhan, F. Wang, M. Safdar and J. He, *Nanoscale*, 2013, **5**, 8326-8339.
23. L. Li, P. A. Salvador and G. S. Rohrer, *Nanoscale*, 2014, **6**, 24-42.
24. Y. Zhao, Y. Zhang, Z. Yang, Y. Yan and K. Sun, *Sci Technol Adv. Mat.*, 2013, **14**, 043501.
25. D. Sarkar, C. K. Ghosh, S. Mukherjee and K. K. Chattopadhyay, *ACS Appl. Mater. Inter.*, 2013, **5**, 331-337.
26. K. Chang, Z. Mei, T. Wang, Q. Kang, S. Ouyang and J. Ye, *ACS Nano*, 2014, **8**, 7078-7087.
27. F. Meng, S. K. Cushing, J. Li, S. Hao and N. Wu, *ACS Catal.*, 2015, **5**, 1949-1955.
28. Y. Li, Y.-L. Li, C. M. Araujo, W. Luo and R. Ahuja, *Catal. Sci. Technol.*, 2013, **3**, 2214.
29. W.-c. Peng and X.-y. Li, *Catal. Commun.*, 2014, **49**, 63-67.
30. D. Hou, W. Zhou, X. Liu, K. Zhou, J. Xie, G. Li and S. Chen, *Electrochim. Acta*, 2015, **166**, 26-31.
31. L. Wei, Y. Chen, Y. Lin, H. Wu, R. Yuan and Z. Li, *Appl. Catal., B*, 2014, **144**, 521-527.
32. D. Wang, Z. Wang, C. Wang, P. Zhou, Z. Wu and Z. Liu, *Electrochem. Commun.*, 2013, **34**, 219-222.
33. B. Pourabbas and B. Jamshidi, *Chem. Eng. J.*, 2008, **138**, 55-62.
34. Q. Liu, Z. Pu, A. M. Asiri, A. H. Qusti, A. O. Al-Youbi and X. Sun, *J Nanopart Res*, 2013, **15**.
35. Q. Xiang, J. Yu and M. Jaroniec, *J. Am. Chem. Soc.*, 2012, **134**, 6575-6578.
36. Y. Zhu, Q. Ling, Y. Liu, H. Wang and Y. Zhu, *Phys. Chem. Chem. Phys.*, 2015, **17**, 933-940.
37. S. Bai, L. Wang, X. Chen, J. Du and Y. Xiong, *Nano Res.*, 2014, **8**, 175-183.
38. H. Liu, T. Lv, C. Zhu, X. Su and Z. Zhu, *J. Mol. Catal. A*, 2015, **396**, 136-142.
39. W. Zhou, Z. Yin, Y. Du, X. Huang, Z. Zeng, Z. Fan, H. Liu, J. Wang and H. Zhang, *Small*, 2013, **9**, 140-147.
40. X. Yu, L. Wang, J. Zhang, W. Guo, Z. Zhao, Y. Qin, X. Mou, A. Li and H. Liu, *J. Mater. Chem. A*, 2015, **3**, 19129-19136.
41. H. W. Wang, P. Skeldon and G. E. Thompson, *Surf. Coat. Tech.*, 1997, **91**, 200-207.
42. J. Zhang, M. Li, Z. Feng, J. Chen and C. Li, *J. Phys. Chem. B*, 2006, **110**, 927-935.
43. J. Zhang, Q. Xu, M. Li, Z. Feng and C. Li, *J. Phys. Chem. C*, 2009, **113**, 1698-1704.
44. M. Shen, Z. Yan, L. Yang, P. Du, J. Zhang and B. Xiang, *Chem. Commun.*, 2014, **50**, 15447-15449.
45. Z. Yin, Z. Zeng, J. Liu, Q. He, P. Chen and H. Zhang, *Small*, 2013, **9**, 727-731.
46. X. Huang, Z. Zeng, S. Bao, M. Wang, X. Qi, Z. Fan and H. Zhang, *Nat. Commun.*, 2013, **4**, 1444.
47. S. H. El-Mahalawy and B. L. Evans, *J. Appl. Crystallogr.*, 1976, **9**, 403-406.
48. D. J. Late, S. N. Shirodkar, U. V. Waghmare, V. P. Dravid and C. N. Rao, *Chemphyschem. A* , 2014, **15**, 1592-1598.
49. J. Pan, G. Liu, G. Q. Lu and H. M. Cheng, *Angew. Chem. Int. Ed.*, 2011, **50**, 2133-2137.
50. Y. Sang, Z. Zhao, J. Tian, P. Hao, H. Jiang, H. Liu and J. P. Claverie, *Small*, 2014, **10**, 3775-3782.
51. D. James and T. Zubkov, *J. Photochem. Photobio. A*, 2013, **262**, 45-51.